On the distortions in calculated GW parameters during slanted atmospheric soundings

Alejandro de la Torre[1], Peter Alexander[2], Torsten Schmidt[3], Pablo Llamedo[1], Rodrigo
Hierro[1]

Correspondence to: Alejandro de la Torre (adelatorre@austral.edu.ar)

[1] Facultad de Ingeniería, Universidad Austral and CONICET, Mariano Acosta 1611, Pilar, Provincia de
Buenos Aires B1629ODT, Argentina

[2] IFIBA, CONICET, Ciudad Universitaria, C1428EGA, Buenos Aires, Argentina

[3] GFZ, GFZ German Research Centre for Geosciences, Section 1.1: GPS/Galileo
Earth Observation, Telegrafenberg A17, D-14473 Potsdam, Germany

Abstract. The significant distortions introduced in the measured atmospheric gravity wavelengths by
soundings other than in vertical and horizontal directions, are discussed as a function of elevation angle of the
sounding path and the gravity waves aspect ratio. Under- or overestimation of real vertical wavelengths
during the measurement process depends basically on the value of these two parameters. The consequences of
these distortions on the calculation of the energy and vertical flux of horizontal momentum are analyzed and
discussed in the context of two experimental limb satellite setups: GPS-LEO radio occultations and
TIMED/SABER measurements. Possible discrepancies previously found between the momentum flux
calculated from satellite temperature profiles, on site and from model simulations, may, to a certain degree, be
attributed to these distortions. A recalculation of previous momentum flux climatologies based on these
considerations seems to be a difficult goal.

1. Introduction

In the last few years, we have observed the ongoing development of several techniques to sound the lower,
middle and upper atmosphere (e.g., Wu and Waters, 1996; Tsuda et al., 2000; Preusse et al., 2002; S.P.
Alexander, et al., 2011; Hertzog et al., 2012; John and Kumar, 2013; Lieberman et al., 2013; Oliver et al.,
2013; M.J. Alexander, 2015; de Wit et al., 2017). The advantages and disadvantages of each choice are
clearly distinguishable among the available rocket-, balloon-, satellite- and satellite-borne instruments, as well
as radar and lidar ground-based devices. Regarding the retrieval of information on atmospheric dynamics
from satellite measurements, we know that both satellite limb and nadir observing techniques are needed to
resolve different parts of the gravity wave (GW) spectrum (Wu et al., 2006) and that a better understanding of

GW complexities requires joint analyses of these data and high-resolution model simulations. The global observation of the atmosphere and the ionosphere using limb or nadir sounding paths, makes it possible to obtain vertical profiles of refractivity, density, temperature (T), pressure, water vapor content and electron density, which is a remarkable achievement obtained with the available experimental resources.

One of the main objectives pursued by current observations is the permanent improvement required in the understanding of GW sources of generation (such as flow over topography, convection, and jet imbalance), as well as their propagation, breaking and dissipation around and above the tropopause, forcing atmosphere circulation. This knowledge, is needed in the sub-grid parameterizations in global models for climate and weather forecasting applications, in order to simulate the influence of orographic and non-orographic GWs and produce realistic winds and temperatures (e.g., Fritts and Alexander, 2003; McLandress and Scinocca, 2005; Kawatani et al., 2009; M.J. Alexander et al., 2010; Shutts and Vosper, 2011; Geller et al, 2013). In these parameterizations, some parameters describe the global distributions of GW vertical flux of horizontal momentum (MF), as well as their wavelengths and frequencies. Until recently, the necessary parameters could not be determined through global observations because the waves are small in scale and intermittent in occurrence. The parameterizations compute a momentum forcing term by making assumptions about the unresolved wave properties that have not been properly constrained by observations. The assumptions are formulated as a set of tuning parameters that are used to adjust the circulation and temperature structure in the upper troposphere and middle atmosphere (M.J. Alexander et al., 2010).

Among recently developed sounding devices, Global Positioning System (GPS) Radio Occultation (RO) is a well-established technique for obtaining global GW activity information. RO uses GPS signals received by Low Earth-Orbiting (LEO) satellites for atmospheric limb sounding. T profiles are derived with high vertical resolution and provide a global coverage under any weather conditions, offering the possibility to carry out the global monitoring of the vertical T structure and atmospheric wave parameters. Several authors have contributed to global analyses of horizontal and vertical GW wavelengths, specific potential energy and MF distribution (Tsuda et al., 2000; de la Torre et al., 2006; Wang and Alexander, 2010; Faber et al., 2013, Schmidt et al. 2016; M.J. Alexander et al. 2015). In particular, P. Alexander et al (2008) (A08) stated that it is not possible to fully resolve GW from RO measurements because there are different kinds of distortions. In each occultation, the outcome depends on wave characteristics (essentially wavelengths and amplitude), the line of sight (LOS) and the line of tangent points (LTP), both with respect to the phase fronts to be detected. Ideal conditions for accurate wave amplitude extraction in occultation retrievals are given by quasi horizontal wave phase surfaces or when the LOS and LTP are respectively nearly contained and out of those planes. Short horizontal scale waves are weakened or even filtered out with high probability. Another result from A08 is that the detected vertical wavelengths will always differ from the original ones, but only the presence of inertio-GWs, which have nearly horizontal constant phase surfaces, will ensure small discrepancies. They concluded that extreme caution is needed when addressing the issues of amplitude, wavelength and phase of gravity waves in occultation data. Some years before A08, de la Torre and P. Alexander (1995) (TA95) already observed and established analytically the discrepancies to be expected between measured and real

horizontal and vertical wavelengths during balloon soundings, taking into account the motion of the gondola with respect to the constant GW phase surfaces. This analysis was performed both from the intrinsic and the ground frame of reference.

In Sect. 2, we analyze in general the distortion to be expected in the detection of real vertical and horizontal wavelengths from almost instantaneous soundings that are different from vertical and horizontal, specifically for satellite measurements. In Sect. 3, the consequences of this distortion in the calculation of GW energy and *MF* are discussed. In Sect. 4, the situation for two satellite setups is considered in some detail. In Sect. 5, some conclusions are outlined for future applications and a possible careful reconsideration of some results and conclusions obtained in previous climatologies is suggested.

2. GW wavelengths distortion

From TA95 and A08, it is clear that when an on site or remote sensing instrument sounds the atmosphere along a given direction, which is different from the vertical or the horizontal plane, the measured vertical and horizontal wavelengths are expected to considerably differ from "real" (or "actual") values. In the Appendix from TA95, 1) a stationary GW observed from 2) a ground-fixed frame of reference (Figure A1 and Eqs. A1-A5) was specifically considered. Now, it may be accepted that both these conditions are emulated by GPS-LEO RO (e.g., Kursinski et al., 1997), as well as by TIMED/SABER (Atmosphere using Broadband Emission Radiometry/Thermosphere-Ionosphere-Mesosphere-Energetics and Dynamics) (Russell et al., 1999) measurements (see below Sect. 4). In relation to the first condition, we may assume that satellite-based soundings yield T profiles almost instantaneously. Following this reasoning, the vertical "real" and "apparent" (or measured) wavelengths (λ_z and λ_z^{ap} respectively) are related by the following expression (TA95, Eq. A3-A5):

$$\lambda_Z^{ap} = \frac{\lambda_Z}{abs(1+\cot(\alpha)\cot(\psi))} \tag{1}$$

where α is the elevation angle defined by a straight sounding path direction and the horizontal plane. In turn, $\cot(\psi)$ is the ratio between the horizontal wavenumber vector ($\boldsymbol{k}_H$) projected on the vertical α - plane, and the vertical wavenumber k_Z (Figure 1). The ratio (k_H / k_Z) is also known as the GW aspect ratio. Fig. 1, with two arbitrary successive GW phase surfaces ϕ_1 and ϕ_2 cutting α-the plane defined, shows a clear difference between real and apparent vertical (and horizontal) wavelengths. This distortion, frequently present in for example radiosoundings or satellite-based GW studies, is in general non negligible and affects the calculation of all magnitudes requiring previous identification of wave parameters.
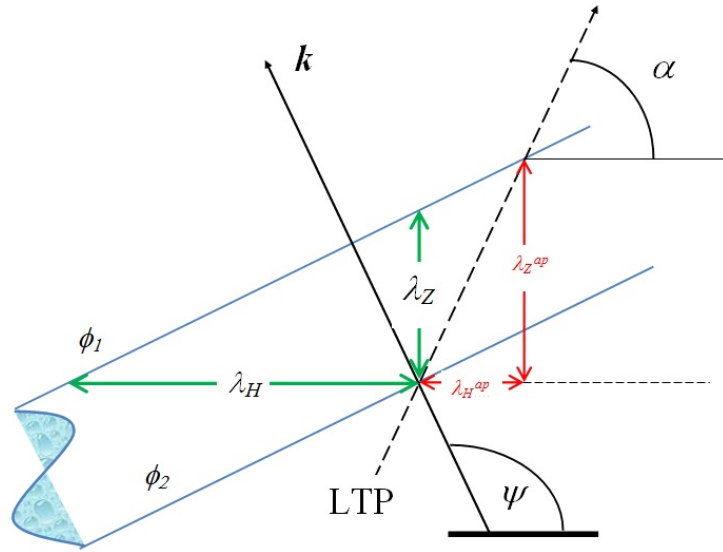
Figure 1: Vertical α-plane defined by the elevation angle between the sounding path direction and its projection on the horizontal plane. Real and apparent vertical and horizontal wavelengths are indicated. ϕ_1 and ϕ_2 represent two arbitrary successive constant phase surfaces belonging to a monochromatic GW (see text). The expected distortion from real to apparent (or measured) wavelengths, is seen.

Here we recall that $\cot(\alpha)$ is equal to the ratio between $\lambda_H{}^{ap}$ and $\lambda_Z{}^{ap}$; this result will be used below. A similar relation to Eq. (1) may be derived between horizontal real and apparent wavelengths, from Eq. A3 to A6 in TA95. The resulting relation is (not shown in TA95):

$$\lambda_H^{ap} = \frac{\lambda_H}{abs(1+\tan(\alpha)\tan(\psi))} \tag{2}$$

We should mention that λ_H is real but may not be the true horizontal wavelength, as information must be sampled along two different horizontal directions, at least to be able to calculate it (e.g. Faber et al 2013, Schmidt et al 2016). We will now focus on the consequences derived from the expected distortion in k_Z or in λ_Z. As is known, in global atmospheric models the subgrid parameterization of GW energy and MF is based on a successful identification of GW parameters, after proper processing of T profiles.

Eq. (1) provides the magnitude of the expected departure in $\lambda_Z{}^{ap}$ from λ_Z, for each monochromatic GW component, within a given wave ensemble at any atmospheric region. In order to better understand this distortion, we will consider this equation as parametric in α or ψ. We recall that, as stated above, both independent parameters are simple trigonometric functions of the apparent and real (horizontal/vertical)

wavenumber components ratio, respectively. The angle α only depends on the sounding path direction during the observation process through progressive atmospheric layers, and ψ, on the GW direction of propagation, $\boldsymbol{k}$ / k. Here, $\boldsymbol{k}$ and k are the wavenumer vector and its absolute value, respectively. We note here that Eq. (1) is symmetric with respect to α and ψ, which are in turn, totally unrelated. For example, in the case of GPS-LEO

125   RO measurements (to be considered below in Sect. 4), α represents the angle defined by the Line of Tangent Points (LTP) and the horizontal plane. In Fig. 1, an arbitrary segment of LTP is roughly represented by a straight line. In this figure we observe, for example, that a vertical sounding of the atmosphere in the nadir direction (i.e., lidar measurements or balloon measurements under zero wind conditions) will produce no distortion at all in k_Z or in λ_Z. The same can be said for horizontal soundings producing no distortions in k_H or

130   in λ_H belonging to the α-plane.

In Fig. 2, we define the distortion as the ratio:

$$D = \frac{\lambda_Z^{ap}}{\lambda_Z} \qquad\qquad (3)$$
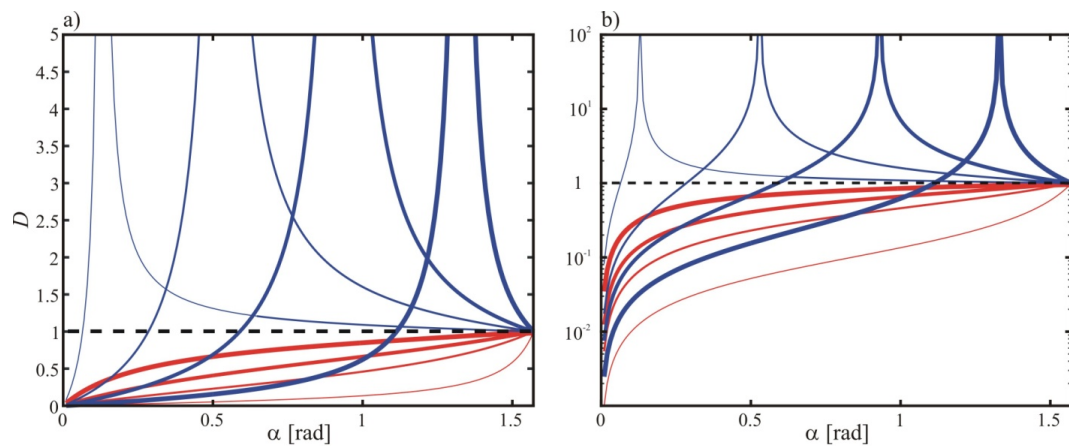
Figure 2: (a) Examples of the distortion in $D = \lambda_Z^{ap} / \lambda_Z$, as a function of α, leaving a parametric dependence

135   with ψ (see text). Arbitrary constant and progressive ψ values within the interval [0, π] rad are shown. Underestimation of λ_Z occurs when ($D < 1$) ψ = 0.1, 0.5, 0.9, 1.3 rad (curves with increasing thickness, from thin red to thickest red, respectively). Overestimation of λ_Z occurs when $D > 1$ and ψ = 1.7, 2.1, 2.5 and 2.9 rad (thin blue to thickest blue curves, respectively). Note that the upper blue branches for $\psi > \pi/2$ diverge at singular values. This is better appreciated in Fig. 2b. The horizontal dashed line corresponds to the "non

140   distortion" case. Considerable general departures from this non distortion limit ($D = 1$) are seen. (b) The same content as in (a), here in linear-log axes.

Following Eq. (1), D may be equivalently represented as a function of α leaving ψ as a parameter, or vice versa, making use of the symmetric dependence on both of them. We first describe this function in terms of α

145   in Fig. 2a and 2b. For illustration, we show the variation of D for increasing selected values of ψ between 0 and π rad. Note that the underestimation of λ_Z occurs when ($D < 1$) $\psi = 0.1$, 0.5, 0.9, 1.3 rad and the overestimation of λ_Z occurs when ($D > 1$) $\psi = 1.7$, 2.1, 2.5 and 2.9 rad. For each ψ value, a singular α value associated to two upper diverging branches is seen. This is better appreciated in Fig. 2b. The horizontal dashed line corresponds to the "non distortion" $D = 1$ case. Considerable general departures from this non-

150   distortion limit are seen. Note that the functional behavior of D is non-symmetric for ψ greater than and less than $\pi/2$ rad. Also, notice that all possible sounding and wave orientations are covered by defining one of the angles between 0 and $\pi/2$ rad and the other one between 0 and π rad.

From the above arguments, we can conclude that for a given GW ensemble, a net significant distortion of the measured spectra should be expected. This net distortion will become more or less significant, depending on

155   i) the composition of the ensemble and ii) the specific measuring device. In the next section we will illustrate this argument for the case of satellite-borne measurements. A 3D plot presents better the functional dependence of D with ψ and α already shown in Fig. 2a-b, now separately for under- and overestimations of $\lambda_{Z,}$ below and above the plane $D = 1$ (Fig. 3a and 3b respectively).

160   a)   b)
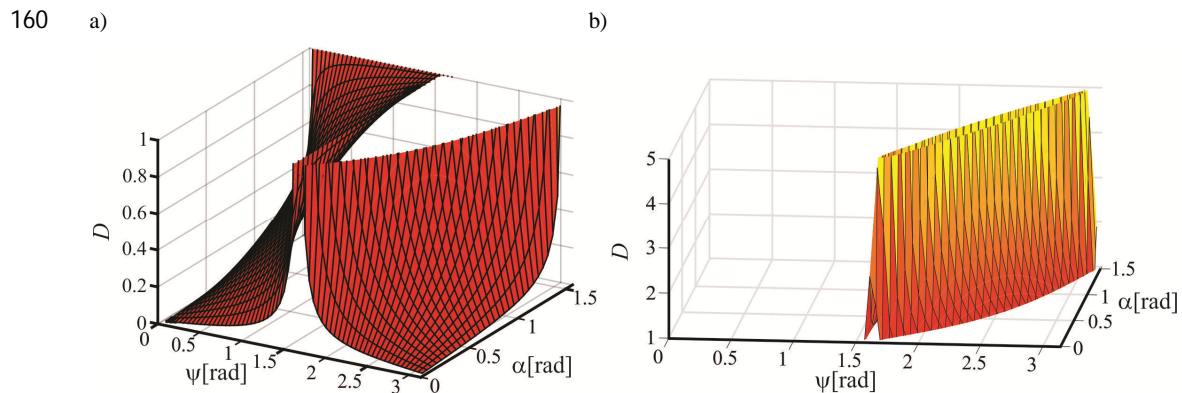
Figure 3: (a) (left) 3D perspective of the distortion D already shown in Figure 2, as a function of ψ and α (see text), for underestimations of λ_Z. (b) (right) The same as in (a), for overestimations of λ_Z. Black lines in this

165   figure are only intended to make easier a visual appreciation of the curved nature of the surfaces.

The 3D plot shows the complete variability of D for a between 0 and $\pi/2$ and ψ between 0 and π. For any fixed ψ value, starting at $\alpha = 0$, each D curve increases from zero, crosses the $D = 1$ boundary diverging at a given α value, located (after/before) $\pi/2$ depending on ψ is (less/greater) than $\pi/2$ and decreases again to

zero, as α approachs the π limit. Due to the symmetric dependance of D with both parameters, to avoid a possible cofusion and redundancy, in Fig. 2 it seems enough to show the D variability for α between 0 and π /2.

3. GW energy, spectra and momentum flux

The computation of the specific potential energy per unit mass, Ep, for a GW ensemble, is given by:

$$Ep = \frac{1}{2}\left(\frac{g}{N}\right)^2 \overline{\left(\frac{\hat{T}}{T_0}\right)^2} = \frac{1}{2}\left(\frac{g}{N}\right)^2 \frac{1}{z_2-z_1}\int_{Z_1}^{Z_2}\left(\frac{\hat{T}}{T_0}\right)^2 dz \qquad (4)$$

Where z_1 and z_2 are the minimum and maximum altitudes for integration, g is the acceleration due to gravity, N is the buoyancy frequency, $\hat{T}$ and T_0 are the perturbation amplitude and background temperature, respectively, and the overbar indicates an averaging process. This average must be performed, for the GW ensemble considered, over at least the largest wavelength in any direction (i.e., horizontal, slanted or, as usually, vertical). Consistently, different choices of this direction involving the same ensemble should ideally yield identical results. Alternatively, the average may be also performed over a time interval at a fixed point, considering a general non-stationary ensemble of GW. In this case, the net contribution of stationary waves would be obviously underestimated. In addition, we recall that the computation of instantaneous Ep at fixed points is sometimes reported without the corresponding averaging process, but we consider that this procedure lacks a clear physical sense.

In Eq. (4) we must previously remove noise and long scale structures in the T profiles. The remaining GWs should include amplitudes expected to significantly contribute to Ep. The vertical interval for integration is usually about 10 km. But, depending on α, ψ_i and the azimuth of each one of the dominant modes in the GW ensemble, some waves may not be contained at least for one complete cycle within the integration interval. Then, the integral in Eq. (4) may not include at least one full wavelength from all these dominant modes. As a result, the individual contribution of each mode to the net Ep will be under- or overestimated to a significant extent.

To extend these considerations to a quite realistic scenario, let us consider the case of a particular modelled distribution of GW vertical wavelengths, selected among the numerous theories developed and based on diverse experimental setups, after the seminal paper by Dewan and Good (1986) (e.g., Smith et al., 1987; Hines, 1991; Fritts and Alexander, 2003; Yiğit et al., 2017, and references therein). It has been observed and broadly assumed, that part of a GW spectrum (the longer vertical wavenumbers) is saturated beyond a given characteristic k_Z^c value that decreases with increasing altitude. Smaller wavenumbers than k_Z^c are not expected to be saturated and their amplitudes increase with increasing altitude. Also, one example of the spectral models proposed to describe the spectral energy density, E, assumes its separability in the product of three functions A, B and C, depending respectively on the vertical wave number, the intrinsic frequency, ω, and the azimuthal direction of propagation, Φ (Fritts and VanZandt, 1993):

$$E(k_Z, \omega, \Phi) = A(k_Z)B(\omega)C(\Phi) = A_0 \frac{1}{\frac{k_Z^c}{k_Z} + \left(\frac{k_Z}{k_Z^c}\right)^3} B(\omega)C(\Phi) \qquad (5)$$

In the above form, $A(k_Z)$ takes into account the requirement of a positive slope (to get a finite vertical energy flux) at small wavenumbers and the proposed k_Z^{-3} dependence at large wavenumber values. This "universal

205 model" has been the subject of several objections and variations in the last three decades (see e.g. Fritts and Alexander, 2003). However we use it here because it serves to illustrate the consequences derived from wavelength and wavenumber distortions. The GW energy contained in a given vertical wavenumber interval Δk_z will be, from Eq. (5), equal to:

$$Ep_{\Delta k_Z} = A_0 B(\omega)C(\Phi) \int_{k_{Z1}}^{k_{Z2}} \frac{1}{\frac{k_Z^c}{k_Z} + \left(\frac{k_Z}{k_Z^c}\right)^3} dk_Z = A_0 B(\omega)C(\Phi) \left[\frac{\tan^{-1}\left(\frac{k_Z^2}{k_Z^{c2}}\right)}{2k_Z^{c-1}} \right]_{k_{Z1}}^{k_{Z2}} \qquad (6)$$

210 Now let us assume that from a given slanted sounding, we detect, after extracting the perturbation with a current wavelet or bandpass filtering analysis, a clearly dominant wave packet, encompassed by two apparent wavenumber bounds. We may calculate the wave energy associated to this wave packet, directly from Eq. (6). In the comparison of this value with the one resulting from the above mentioned (or any other) model, Eq. (6) provides an idea of the distortion in E_p to be expected. This will occur when the above integration limits, are

215 wrongly replaced by $k_Z^{ap}{}_{(1,2)}$, instead of:

$$k_{Z\,(1,2)} = k_{Z\,(1,2)}^{ap} abs(1 + \cot(\alpha)\cot(\psi)) \qquad (7)$$

To simplify the argument, as an approximation to the net E_p distortion, here we assumed a parametric dependence both in α and in ψ, despite the fact that these are functions of real and apparent wavelengths.

After these considerations, we recall that the *MF* for internal GWs may be calculated under certain hypotheses

220 based on the existence of a dominant mode within a given intrinsic frequency range, applying the following equation (for its detailed derivation and discussion refer to Appendix A of Ern et al. (2004)):

$$MF = \frac{\rho}{2} \frac{\lambda_Z}{\lambda_H} \left(\frac{g}{N}\right)^2 \overline{\left(\frac{\hat{T}}{T_0}\right)^2} = \rho \frac{\lambda_Z}{\lambda_H} Ep \qquad (8)$$

where ρ is the background density. As stated before, the ratio $\lambda_Z^{ap}/\lambda_H^{ap}$ is equal to $\cot(\alpha)$. In the calculation of the *MF*, a replacement in Eq. (8) of apparent instead of real wavelengths, would absurdly lead to the fact

225 that the *MF* changes according to the geometry of the sounding path. Even obtaining λ_H^{ap} from horizontal 2D information would not eliminate the problem of using λ_Z^{ap} instead of λ_Z.

To provide a quantification of the distortion in *MF* using specific data, we consider a case study close to Alpes mountains analyzed in detail by Hierro et al. (2017, submitted to this AMT issue –in what follows H17). In that case study, from a collocation database between RO and cloud data and from Weather Research

230 and Forecasting (WRF) mesoscale model simulations, real and apparent vertical wavelengths during COSMIC RO soundings were clearly identified. From the model, coherent bi-dimensional GW structures with constant phase surfaces oriented along S-N direction and slightly tilted to N-E with increasing latitude, were noted. From the orographic quasi monochromatic structures detected below the cloud tops, $\lambda_Z \approx 15$ km and λ_H = 20 km were estimated, yielding the ratio $\lambda_Z/\lambda_H = 0.75$ with a wave propagation angle $\psi = \tan^{-1}(\lambda_H/\lambda_Z) \approx$

235 0.93 rad. We recall that in Sec. 2 we mentioned that α may be calculated from a rectilinear approximation of the LTP and cot (α) is also equal to the ratio between λ_H^{ap} and λ_Z^{ap} in the region and altitude interval considered in H17. From the average inclination of LTP, $\alpha = \lambda_H^{ap} / \lambda_Z^{ap} \approx 0.23$, which differs considerably from the ratio between the corresponding real wavelengths. From Eq. (8) the proportionality of *MF* to the real wavelengths ratio indicates that if this ratio is errornously replaced by the apparent ratio, a relative error of

240 70% is, in this case, introduced. The second source of error is additionally introduced through *Ep*. An estimation of its relative error may be derived replacing apparent instead of real limits of integrations in Eq. (6), assuming the simplified proposed spectral model:

$$\frac{\Delta Ep_{\Delta k_Z}}{Ep_{\Delta k_Z}} = \left\{ \left[\frac{\tan^{-1}\left(\frac{k_Z^2}{k_Z^{c\,2}}\right)}{2k_Z^{c\,-1}} \right]_{k_{Z1}}^{k_{Z2}} - \left[\frac{\tan^{-1}\left(\frac{k_Z^2}{k_Z^{c\,2}}\right)}{2k_Z^{c\,-1}} \right]_{k^{ap}_{Z1}}^{k^{ap}_{Z2}} \right\} / \left[\frac{\tan^{-1}\left(\frac{k_Z^2}{k_Z^{c\,2}}\right)}{2k_Z^{c\,-1}} \right]_{k_{Z1}}^{k_{Z2}} \qquad (9)$$

This value will obviously depend on the corresponding characteristic parameter value. The net relative MF

245 relative error will then be given by the sum of of both errors.

4. Distortion of vertical wavelengths for specific setups

To illustrate the considerations from Sect. 2 and 3, let us consider the *T* retrievals obtained from 1) RO events detected from different LEO-GPS satellites and from 2) SABER/TIMED measurements. A GPS-LEO RO

250 occurs whenever a transmitting satellite from the global navigation network at an altitude about 20,000 km rises or sets from the standpoint of a LEO receiving satellite at a height of about 800 km and the signal goes across the atmospheric limb. The doppler frequency alteration produced through refraction of the ray by the Earth's atmosphere in the trajectory between the transmitter and the receiver is detected and then may be converted into slant profiles of diverse variables in the neutral atmosphere and the ionosphere. GPS-LEO RO

255 observations available since 2001 have been broadly used to study global distributions of GW energy and momentum, mainly in the troposphere and the stratosphere (e.g. de la Torre et al., 2006; Alexander et al.2010; Geller et al., 2013; Schmidt et al., 2016). The RO technique is a global limb sounding technique, sensitive under all weather conditions to GW with small ratios of vertical to horizontal wavelengths (Wu et al., 2006, P. Alexander et al., 2016). The SABER/TIMED limb measurements provided continuous global *T* data for the

260 latitude range 50°N–50°S from the lower stratosphere to the lower thermosphere and represent an

unprecedented opportunity for studying in detail the atmospheric waves, in particular GW, as well as their role in lower and upper atmosphere coupling (e.g., Pancheva et al., 2011). The TIMED satellite provides observations since January 2002. It measures CO_2 infrared limb radiance from approximately 20 to 120 km altitude. Kinetic temperature profiles are retrieved over these heights using local thermodynamic equilibrium
265   (LTE) radiative transfer in the stratosphere and lowest part of the mesosphere (up to 60 km) and a full non-LTE inversion in the mesosphere and lower termosphere (i.e., Mertens et al., 2004; Pancheva and Mukhtarov, 2011).

In Fig. 4a and 4b, LTPs corresponding to both setups are illustratively shown, for the higher tropospheric and lower stratospheric regions bounded by 31◦S-37◦S and 66◦W-72◦W, close to central southern Andes
270   mountains, during January-February 2009.
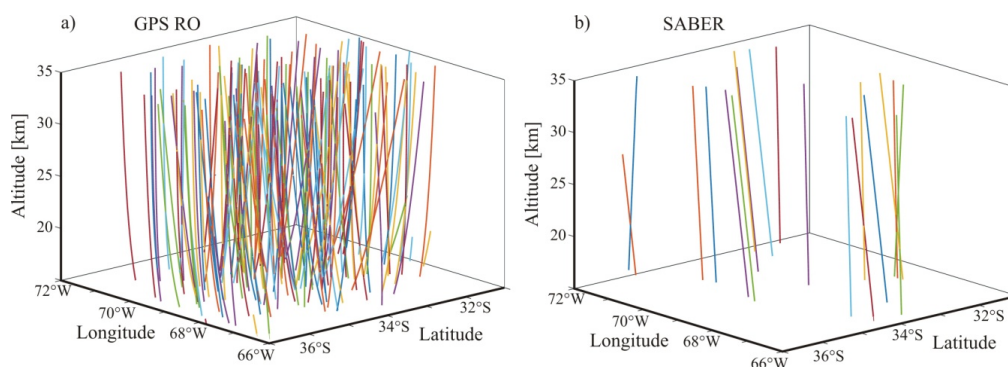
Figure 4: (a) LTPs corresponding to available profiles during the period Jan-Feb 2009, retrieved from tropo-
275   stratospheric GPS-RO events (see text). (b) The same as (a), for SABER measurements. Arbitrary colors were included to make easier the visual inspection.

Keeping in mind the difference between horizontal and vertical scales in these figures, a typical dispersion of the sounding path direction (α) among GPS-RO occultation events and among SABER measurements, is
280   observed. The large number of available RO as compared to SABER profiles is evident. The approximation of the sounding paths by straight segments seems, at least for our purpose here, quite reasonable. Let us now consider the global data retrieved from both setups during January-February 2009 (RO from LEOs: SAC-C, CHAMP, MetOp-A, and COSMIC), of which Fig. 4 only represents a regional subset. In Fig. 5a and 5b the α distribution is shown. Here a linear interpolation was applied to the weakly variable α angle in each RO
285   event, between the lowest and upper available LTP values. Note the considerably narrower variability α-range among SABER profiles. We did not observed remarkable differences in the general latitudinal or

geographical distribution. The possible ranges observed from both experimental setups allow some preliminary consequences to be drawn regarding the expected wavelength distortions. For example, for the subset in Fig. 4, we know that very close to the Andes mountains region, dominant large-amplitude, stationary

290 and non hydrostatic GWs are usually observed (de la Torre et al., 1996, 2005, 2015).
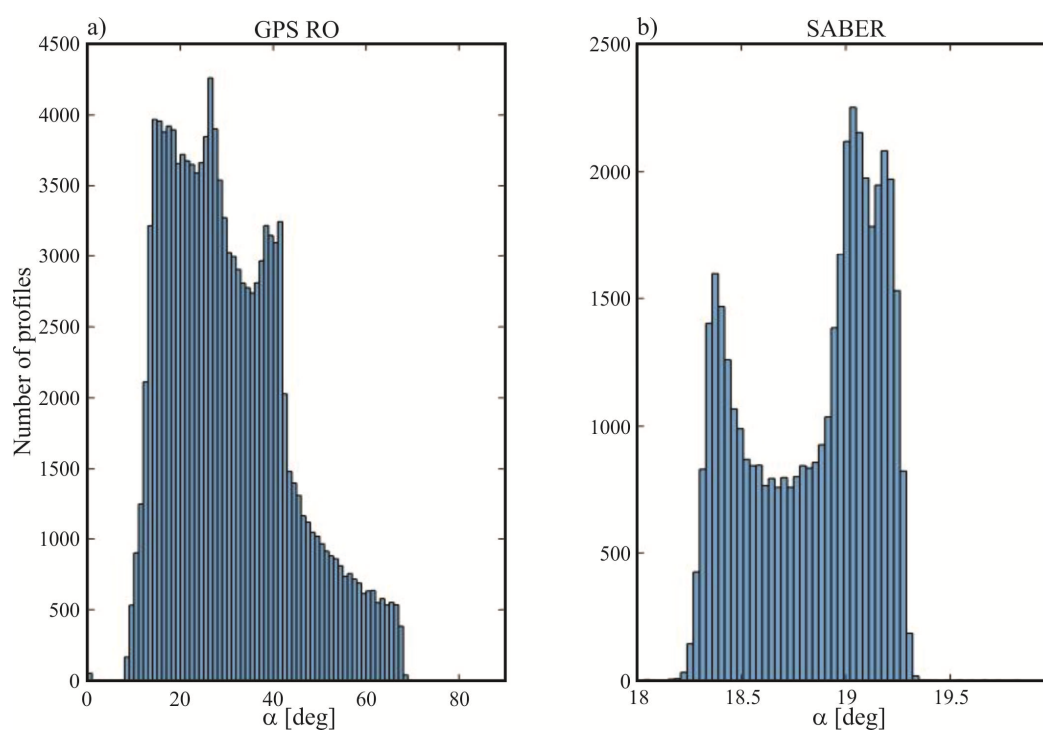
Figure 5: Distribution of available profiles with elevation angle between the sounding path direction and the
295   horizontal plane, globally retrieved, during the period Jan-Feb 2009 from a) GPS-LEO RO and b)
TIMED/SABER measurements (see text).

Accordingly, large GW aspect ratios may be expected there (Gill, 1982). On the other hand, at tropical latitudes, where convective GWs dominate the scenario, or even close to polar jet regions where hydrostatic

300 rotating or non rotating GWs are usually found, considerably lower characteristic aspect ratios should be dominant. In Fig. 6, we reproduce the D-α curves selected in Fig. 2a and 2b, for successive ψ values ($\Delta\psi$ step = 0.2), now adding in dash-dotted green and yellow squares, the D-α ranges affected for both experimental setups. These ranges are, respectively, [0.17-1.22] rad for GPS-RO and [0.32-0.34] rad for SABER. For each

setup, the relevant difference mainly depends on whether α and ψ belong to the same or different

305    $[0, \pi/2]$ and $[\pi/2, \pi]$ intervals.
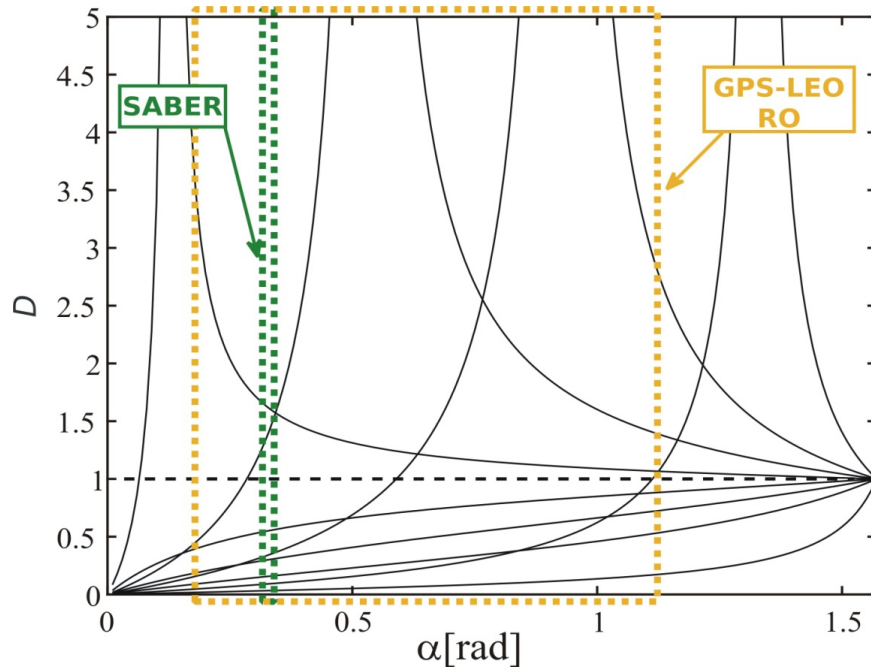
Figure 6: The α ranges corresponding to both experimental setups, are defined within dash-dotted colored boxes. These ranges are [0.17-1.22] rad and [0.32-0.34] rad, respectively in yellow and green, for GPS-RO and SABER, according to Fig. 5. The curves already selected in Fig. 2a and 2b for successive and constant

310   ψ values ($\Delta\psi$ step= 0.4) between 0.1 and 2.9, are included in black for reference purposes.

Here, we may here observe that depending on GW aspect ratio and sounding direction, general under and overestimations of λ_Z are both possible throughout both experimental setups. Within a given ensemble, the behavior of D for ψ lower and greater than $\pi/2$ is different. This suggests that different modes in the

315   ensemble may show individual distortions less than or greater than 1. Then, some compensations contributing to Ep and MF are expected from different modes in the ensemble, but the net distortion should still be considerable. In Fig. 7, the D-ψ constraint imposed to GPS-RO observations, now for constant and progressive α values, is shown. $\Delta\alpha$ steps of 0.02 rad and within the corresponding bounds [0.17-1.22] rad indicated in Fig. 5, are shown. The white, light grey and grey sectors approximately indicate the non-

320   hydrostatic, hydrostatic non-rotating and hydrostatic rotating GW regimes, respectively. We observe general underestimations for ψ less than $\pi/2$ and in the vicinity of π rad. Between these sectors, under and overestimations are possible. To illustrate the consequences on a realistic and simple scenario, let us consider

again the region situated to the east of the central Andes, mentioned in Figures 4a and 4b. Let us suppose that, consistently with observations and numerical simulations (i.e., de la Torre et al., 2012; Jiang et al., 2013;
325 Fritts et al., 2015), constant and stationary GW phase surfaces exhibit a systematic inclination with respect to the ground and a high aspect ratio, following the almost omnipresent forcing by mean westerlies at the mountain tops. This feature is represented in Fig. 7 by the black arrow.
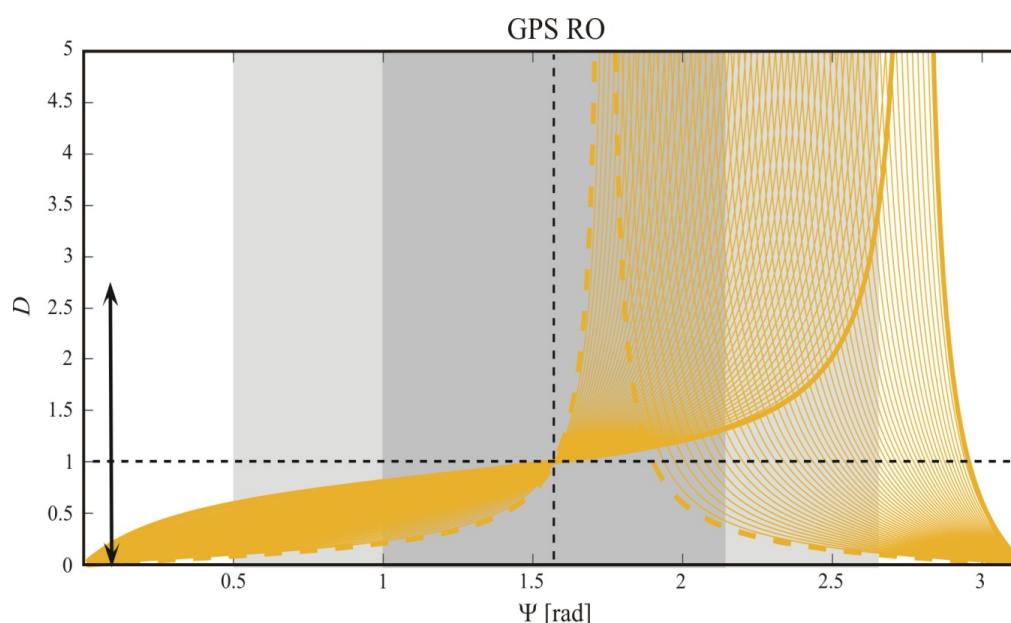
330 Figure 7: The yellow curves represent progressive and constant selected α values (step $\Delta\alpha = 0.02$ rad). They are selected within the allowed bounds [0.17-1.22] rad in the D-ψ GPS RO region, according to Figure 5. These lower and higher bounds are indicated by thick dotted and full lines, respectively. White, light grey and grey sectors roughly indicate the non-hydrostatic, hydrostatic non-rotating and hydrostatic rotating GW regimes, respectively. Both quadrants are separated by the vertical dashed curve. The black double arrow
335 indicates an hypothetical dominant non-hydrostatic GW that may be observed at different α directions, from different GPS-LEO satellites pairs. The "forbidden GPS-LEO RO sectors" are any sectors excepting those covered by yellow lines.

This arrow spans over all possible α directions within the bounds imposed by the geometry of every GPS-
340 LEO satellites combination during each occultation event. This assumed scenario would reveal a net underestimation of λ_Z, regardless of the inclination of LTPs during the sounding of the region and the considered period. In general the analysis is expected to be more complex, given distinct LTPs contributions

that may under- and overestimate λ_Z. Finally, Figure 8 indicates the corresponding D-ψ features for SABER measurements, similarly as in Figure 7.

345
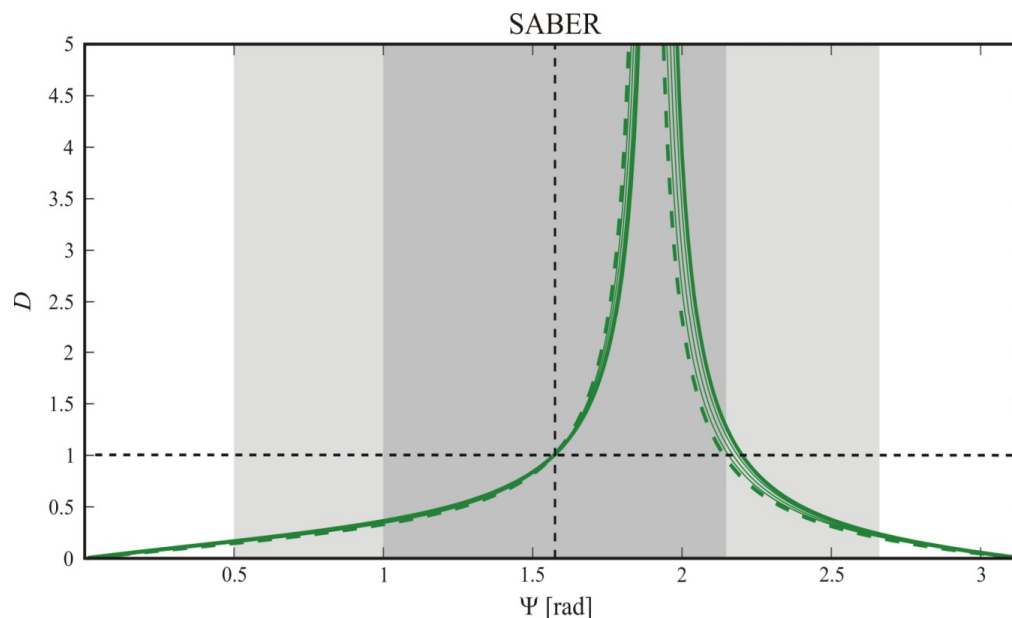
Figure 8: The same as Fig. (7), here for SABER measurements, within the considerably narrower α bounds [0.32-0.34] rad than for the GPS-RO setup, according to Fig. (5). These lower and higher bounds are indicated by thick dotted and full green lines, respectively. The "forbidden SABER sectors" are any sectors excepting those covered by green lines.

350

Here we observe general underestimations for ψ, along the 3 GW regimes, for values less than $\pi/2$ and greater than around 2.3 rad. For intermediate values, only overestimations are expected. Note that for SABER measurements, the forbidden D-ψ region is considerably more extended than for GPS-LEO RO measurements.

355

5. Discussion and conclusions

The expected distortions undergone in the measured vertical wavelengths during any almost instantaneous slanted atmospheric sounding, as may be the case for satellite instruments, is discussed. For the particular case of vertical or horizontal soundings, we know that no distortion is expected in λ_Z and $\lambda_{H,}$ respectively.

360   The features observed are described as a function of GW aspect ratio and the inclination of the sounding path.

To gain a better understanding of this distortion, and making use of the symmetric D dependence with α and ψ, we consider the expression for D as a parametric equation in both independent variables. To illustrate the constraints imposed to both parameters by applying different instrumental setups and GW scenarios, we show the results conveniently in D-α and D-ψ plots. Above and below the non-distortion limit ($D = 1$), general under and overestimations occur depending on the relative parametric values. The main difference is produced by two possible situations: α and ψ belonging to the same or different quadrants, taken from $[0, \pi/2]$ and $[\pi/2, \pi]$. Given a GW ensemble and a number of measurements within arbitrary space bounds and time intervals, distinct wavelength under- and overestimations should be expected.

When Ep is calculated over a GW ensemble in any individual T profile, an integral must be performed over the largest wavelength along any chosen direction. The selection of the upper and lower vertical wavelength bounds, should include those prevailing GW amplitudes expected to mostly contribute to Ep. Depending on α and the respective ψ values for each one of the dominant GW modes, some dominant real wavelengths may not be fully contained within the integration interval. The integral in Ep then will not include at least one wavelength of every dominant mode. The Ep calculation could be under- or overestimated up to a significant extent.

We illustrate these arguments in an approximately real scenario considering a modelled distribution of GW. This is based on the usual saturation of large vertical wavenumbers and in the separability of the spectral function in the vertical wave number, the intrinsic frequency and the azimuthal direction of propagation. To calculate the wave energy associated to a given GW packet within an ensemble, we use a simple analytical result derived from the spectral model to get an idea of the distortion expected by wrongly replacing the integration limits by apparent instead of real wavenumber values. This (or any) distortion in Ep will in turn be translated to the MF, by applying a previous result obtained by Ern et al. (2004). In addition, through a multiplying factor, the MF would be then illogically dependent on the inclination angle of the sounding path.

The results are considered for two specific experimental setups: GPS-RO and SABER measurements. For our analysis we approximate the sounding paths in both cases by straight segments. The relevance of this assumption was assessed. A clearly larger number of available T profiles is seen from RO events. The α ranges in both techniques allow to define forbidden regions in D-α as well as in D-ψ diagrams, relative to the different GW aspect ratios (the non-hydrostatic, hydrostatic non-rotating and hydrostatic rotating regimes). Within a given GW ensemble, even expecting some compensation when D is less than and greater than 1, the net distortion effect, as well as its contribution to Ep and MF, should be considerable. With the exception of GWs with prevailing high aspect ratio, as for example near the Andes mountains where a net underestimation of λ_z should be observed, under- and overestimatons are in general expected, from both setups respectively. This occurs for T profiles where α and ψ belong to the same or different quadrants $[0, \pi/2]$ and $[\pi/2, \pi]$. For SABER measurements, the forbidden D-ψ region is considerably more extended than the one corresponding to the GPS-RO measurements.

In the global study of Geller et al. (2013), which compares models with diverse parameterizations with satellite and balloon data, the faster fall off with height of the gravity wave *MF* derived from satellite measurements than in the models considered in that study was the most significant discrepancy between measured and model fluxes. These authors concluded that the reasons for those differences remain unknown,

400 although various explanations for the differences were proposed. As we know, from model simulations the *MF* is not computed from Eq. (8), but from its formal definition, based on the average of the products of the three perturbed components of the air velocity. Based on the above considerations and regarding the dramatic distortions on vertical and horizontal wavelengths during slanted soundings, we may infer that if *MF* is computed from Eq. (8), the wavelengths distortion will unavoidably be translated to the calculation of *MF*.

405 Obviously, this situation must be considered together with the additional constraints imposed to any satellite-borne observational window, largely discussed by several authors, including A08. Finally, we must admit that the global calculation of *MF* from slanted *T* profiles including all necessary corrections, even assuming quasi monochromatic GW packets, appears to be a very complex task. The distortions described above are only avoided in the calculation of *MF* if the atmosphere is sounded in the vertical or horizontal directions, as

410 provided (but only locally) by lidar/radar and balloon setups, respectively.

Acknowledgements

The study has been supported by the CONICET under grants CONICET PIP 11220120100034 and ANPCYT

415 PICT 2013-1097 and by the German Federal Ministry of Education and Research (BMBF) under grant 01DN14001.

References

420

Alexander, M. J.: Global and seasonal variations in threedimensional gravity wave momentum flux from satellite limb-sounding temperatures, Geophys. Res. Lett., 42, 6860–6867, doi:10.1002/2015GL065234, 2015.

Alexander, M. J., Geller, M., McLandress, C., Polavarapu, S., Preusse, P., Sassi, F., Sato, K., Eckermann, S., Ern, M., Herzog, A., Kawatani, Y., Pulido, M., Shaw, T. A., Sigmond, M., Vincent, R., and Watanabe, S.:

425 Recent developments in gavity-wave effects in climate models and the global distribution of gravity wave momentum flux from observations and models, Q. J. Roy. Meteorol. Soc., 136, 1103–1124, doi:10.1002/qj.637, 2010.

Alexander, P., de la Torre, A., Llamedo, P.: The interpretation of gravity waves signatures extracted from GPS radio occultations. J. Geophys. Res., 113, D16117, doi:10.1029/2007JD009390, 2008.

430   Alexander, P., de la Torre, A., Hierro, R., Llamedo, P.: An improvement of the sensitivity of GPS radio occultation data to detect gravity waves through observational and modeling factors, Adv. Space Res., 57, 543–55, 2016.

Alexander, S. P., Klekociuk, A.R., Murphy, D.J.: Rayleigh lidar observations of gravity wave activity in the winter upper stratosphere and lower mesosphere above Davis, Antarctica (69°S, 78°E), J. Geophys. Res., 116, 435   D13109, doi:10.1029/2010JD015164, 2011.

de la Torre, A. and Alexander, P.: The interpretation of wavelengths and periods as measured from atmospheric balloons, J. Appl. Meteor., 3•, 2747-2754, 1995.

de la Torre A., H. Teitelbaum, H., Vial, F.: Stratospheric and tropospheric gravity wave measurements near the Andes Mountains, J. Atmos. Terr. Phys., 58, 521-530, 1996.

440   de la Torre A and Alexander, P.: Gravity Waves above Andes Detected from GPS Radio Occultation Temperature Profiles: Mountain Forcing?, Geophys. Res. Lett., 32, 17, L17815, 10.1029/2005GL022959, 2005.

de la Torre A., Alexander, P., Llamedo, P., Menéndez, C., Schmidt, T., Wickert, J.: Gravity Waves above Andes Detected from GPS Radio Occultation Temperature Profiles. II: Jet Mechanism?, Geophys. Res. Lett, 445   33, L24810, doi:10.1029/2006GL027343, 2006.

A. de la Torre, A.; Alexander, P.; Hierro, R.; Llamedo, P; Rolla, A; Schmidt, T.; Wickert, J. Large Amplitude Gravity Waves above the Southern Andes, the Drake Passage and the Antarctic Peninsula. J: Geophys. Res., 117, D2, doi:10.1029/2011JD016377, 2012.

de la Torre, A., Pessano, P., Hierro, R., Santos, J.R., Llamedo, P., Alexander, P.: The influence of topography 450   on vertical air velocity of air in relation to severe storms near the Southern Andes Mountains, Atmosph. Res., doi: 10.1016/j.atmosres.2014.12.020156, 2015.

de Wit, R. J., Janches, D., Fritts, D.C., Stockwell, R.G., Coy, L.: Unexpected climatological behavior of MLT gravity wave momentum flux in the lee of the Southern Andes hot spot, Geophys. Res. Lett., 44, doi:10.1002/2016GL072311, 2017.

455   E. M. Dewan, Good, R.E.: Saturation and the "universal" spectrum for vertical profiles of horizontal scalar winds in the atmosphere, J. Geophys. Res., Volume 91, D2, 2742–2748, 1986.

Ern, M., Preusse, P., Alexander, M.J., Warner, C.D.: Absolute values of gravity wave momentum flux derived from satellite data, J. Geophys. Res., 109, D20103, doi:10.1029/2004JD004752, 2004.

Faber, A., Llamedo, P., Schmidt, T., de la Torre, A., Wickert, J.: A New Approach to Global Gravity Wave
460   Momentum Flux Determination from GPS Radio Occultation Data, Atmos. Meas. Tech. Dis.,
doi:10.5194/amtd-6-2907-2013, 2013.

Fritts, D. C., and VanZandt, T.E.: Spectral estimates of gravity wave energy and momentum fluxes, I, Energy
dissipation, acceleration, and constraints, J. Atmos. Sci., 50, 3685–3694, 1993.

Fritts, D. C., Alexander. M.J.: Gravity wave dynamics and effects in the middle atmosphere, Rev. Geophys.,
465   41(1), 1003, doi:10.1029/2001RG000106, 2003.

Fritts, D.C. et al,: The Deep Propagating Gravity Wave Experiment (DEEPWAVE): An Airborne and
Ground-Based Exploration of Gravity Wave Propagation and Effects from Their Sources throughout the
Lower and Middle Atmosphere, BAMS, DOI: http://dx.doi.org/10.1175/BAMS-D-14-00269.1, 2016.

Geller, M. A., et al.: A comparison between gravity wave momentum fluxes in observations and climate
470   models, 26, 6383–6405, doi:10.1175/JCLI-D-12-00545.1., 2013.

Gill, A.E.: Atmosphere and Ocean Dynamics, Academic Press, New York, 642 pp, 1982.

Hertzog, A., Alexander, M.J., Plougonven, R.: On the intermittency of gravity wave momentum flux in the
stratosphere, J. Atmos. Sci., 69, 3433-3448, doi:10.1175/JAS-D-12-09.1, 2012.

Hierro, R., Steiner, A.K., de la Torre, A., Alexander, P., Llamedo, P., Cremades, P.: Orographic and
475   convective gravity waves above the Alps and Andes mountains during GPS radio occultation events – a case
study, submitted to Atmos. Meas. Tech., 2017.

Hines, C. O., The saturation of gravity waves in the middle atmosphere, part I, Critique of linear-instability
theory, J.Atmos. Sci., 48, 1348–1359, 1991.

Jiang, Q., Doyle, J.D., Reinecke, A., Smith, R.B., Eckermann, S.D.: A modeling study of stratospheric waves
480   over the Southern Andes and Drake Passage, J. Atmos. Sci., 70, 1668–1689, doi:10.1175/JAS-D-12-0180.1,
2013.

John, S. R., and Kumar, K.K.: A discussion on the methods of extracting gravity wave perturbations from
space-based measurements, Geophys. Res. Lett., 40, 2406–2410, doi:10.1002/grl.50451, 2013.

Kawatani, Y., Takahashi, M., Sato, K., Alexander, S.P., Tsuda, T.: Global distribution of atmospheric waves
485   in the equatorial upper troposphere and lower stratosphere: AGCM simulation of sources and propagation, J.
Geophys. Res., 114, D01102, doi:10.1029/2008JD010374, 2009.

Kursinski, E. R., Hajj, G.A., Hardy, K.R., Schofield, J.T., Linfield, R.: Observing Earth's atmosphere with radio occultation measurements using the Global Positioning System, J. Geophys. Res., 102, 23,429– 23,465, 1997.

490 Lieberman, R. S., Akmaev, R.A., Fuller-Rowell, T.J., Doornbos, E.: Thermospheric zonal mean winds and tides revealed by CHAMP, Geophys. Res. Lett., 40, doi:10.1002/grl.50481, 2013.

McLandress, C., and Scinocca, J.F.: The GCM response to current parameterizations of nonorographic gravity wave drag, J. Atmos. Sci., 62, 2394–2413, 2005.

Mertens, C.J. et al.: SABER observations of mesospheric temperature and comparisons with falling sphere 495 measurements taken during the 2002 summer MaCWINE campaign. Geophys Res Lett 31:J03105. doi:10.1029/2003GL018605, 2004.

Oliver, W. L., Zhang, S.-R., Goncharenko, L.P.: Is thermospheric global cooling caused by gravity waves?, J. Geophys. Res. Space Physics, 118, doi:10.1002/jgra.50370, 2013.

Pancheva, D., Mukhtarov, P., Andonov, B., Mitchell, N.J., Forbes, J.M.: Planetary waves observed by 500 TIMED/SABER in coupling the stratosphere-mesospherelower thermosphere during the winter of 2003/2004: Part 1 comparison with the UKMO temperature results. J. Atmos. Sol. Terr. Phys. 71, 61–74. http://dx.doi.org/10.1016/j.jastp.2008.09.016, 2009.

Preusse, P., Dörnbrack, A., Eckermann, S.D., Riese, M., Schaeler, B., Bacmeister, J.T., Broutman, D., Grossmann, K.U.: Space-based measurements of stratospheric mountain waves by CRISTA, 1. Sensitivity, 505 analysis method, and a case study, J. Geophys. Res., 107(D23), 8178, doi:10.1029/2001JD000699, 2002.

Russell III, J.M., Mlynczak, M.G., Gordley, L.L., Tansock, J., Esplin, R.: An overview of the SABER experiment and preliminary calibration results. Proceedings of the SPIE, 44th anual meeting, Denver, CO, 18–23 July: v. 3756, pp 277–288, 1999.

Schmidt, T., Alexander, P., de la Torre, A.: Stratospheric gravity wave momentum flux from radio 510 occultations, J. Geophys. Res. Atmos., 121, 4443–4467, doi:10.1002/2015JD024135, 2016.

Smith, S. A., Fritts, D.C., VanZandt, T.E.: Evidence for a saturated spectrum of atmospheric gravity waves, J. Atmos.Sci., 44, 1404–1410, 1987.

Shutts, G.J., Vosper, S.B.: Stratospheric gravity waves revealed in NWP model forecasts. Q. J. R.Meteorol. Soc. 137: 303–317. DOI:10.1002/qj.763, 2011.

515   Tsuda, T., Nishida, M., Rocken, C., Ware, R. H.: A global morphology of gravity wave activity in the stratosphere revealed by the GPS occultation data (GPS/MET), J. Geophys. Res., 105, 7257–7273, doi:10.1029/1999JD901005, 2000.

Wang, L., and Alexander, M.J.: Gobal estimates of gravity wave parameters from GPS radio occultation temperature data, J. Geophys.Res., 115, D21122, doi:10.1029/2010JD013860, 2010.

520   Wu, D. L., et al.: Remote sounding of atmospheric gravity waves with satellite limb and nadir techniques, Adv. Space Res., 37, 2269–2277, 2006.

Wu, D.L. and Waters, J.W.: Satellite observations of atmospheric variances: A possible indication of gravity waves, Geophys. Res. Lett., 23, 3631– 3634, 1996.

Yiğit, E., Knížováb, P., Georgieva, K., Ward, W.E.: A review of vertical coupling in the Atmosphere–
525   Ionosphere system: Effects of waves, sudden stratospheric warmings, space weather, and of solar activity, J. Atmos. Sol-Terr. Phys., http://dx.doi.org/10.1016/j.jastp.2016.02.011 1364-6826/2016, 2017.